Experiments on the transition of thermocapillary bubble convection towards turbulent flow

Ebram Tadrous [1,2,*] and Günter Wozniak [1,3,†]

[1] *Chair of Fluid Mechanics, Institute of Mechanics and Thermodynamics, Faculty of Mechanical Engineering, Chemnitz University of Technology, Reichenhainer Str. 70, D-09107 Chemnitz, Germany*

[2] *Chair of Mechanical Power Engineering, Faculty of Engineering, Cairo University, Giza, Egypt*

[3] *SUVIS GmbH Altchemnitzer Str. 11, D-09120 Chemnitz, Germany*

(Received 15 November 2020; accepted 21 April 2021; published 1 June 2021)

Thermocapillary-driven convection around an air bubble immersed in a liquid matrix under a heated wall is experimentally investigated under gravitational conditions. This work explores the thermocapillary convective flow behavior under conditions beyond the steady state towards turbulent flow. The phenomenon is basically studied through the visualization of the fluid flow and its structure around the interface of an injected air bubble subjected to an upward temperature gradient. The flow is qualitatively categorized according to the transient behavior of the thermocapillary vortex boundary contour around the bubble using the shadowgraph technique. The volatility of the low-viscosity silicone oil as test fluid restricts the maximum flow temperature to 53 °C to avoid the formation of disruptive vapor bubbles. However, the introduction of experiments under excess pressure conditions facilitates studying the impact of higher flow driving temperature gradients while greatly reducing the distortion effect. Both periodic and nonperiodic oscillations of the liquid flow around the bubble have been observed. Also, symmetric and nonsymmetric periodic fluid flow oscillations were recorded depending on different interfacial boundary conditions due to the bubble volumes and the applied temperature gradient. These periodic oscillations were distinguished from the nonperiodic ones through the behavior of the thermocapillary vortex boundary contour. The values of the transitional Marangoni number $\mathrm{Mg}_{\mathrm{tran}}$, where the liquid flow evolves into a nonperiodic state, could be achieved at different bubble aspect ratios r_B/z_B. Four different nonperiodic flow modes surrounding the bubble periphery have been identified within the nonperiodic flow regime. Our study reveals, that under appropriate conditions, a surface-tension-driven (thermocapillary) flow can become turbulent.

DOI: 10.1103/PhysRevFluids.6.063601

I. INTRODUCTION

Temperature gradients in liquid-gas and immiscible liquid-liquid systems can evolve both free and forced convection influencing heat and mass transfer processes within the system. Under gravitational conditions, convective flow due to buoyancy is dominant as a result of density variations caused by temperature gradients. Moreover, a secondary convective flow can be observed at the phase boundary (interface) between a liquid and a gas or two immiscible liquids. This additional convective flow is a result of surface tension gradients at the phase boundary. The variation of interfacial tension with temperature, $\partial\sigma/\partial T$, caused by interfacial temperature gradients

*tadrousebram@gmail.com

†guenter.wozniak@mb.tu-chemnitz.de

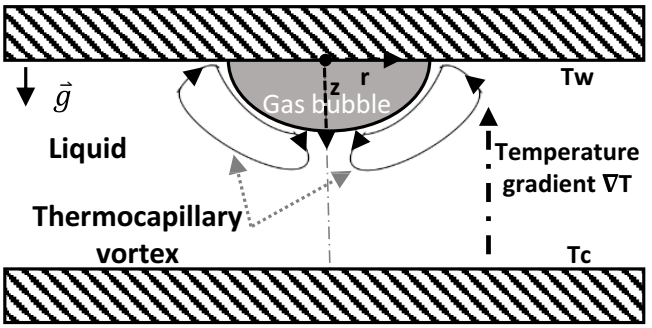

FIG. 1. Schematic of thermocapillary bubble convection under a heated wall.

$|\partial T/\partial z|$ leads to a fluid flow towards regions of high surface tensions and low temperatures, termed thermocapillary or Marangoni convection. The physical problem can be distinguished by a dimensionless number which represents the relative importance of convective heat transport induced by thermocapillary convection when compared to the molecular heat transfer, referred to as the Marangoni number Mg. Since the early observations [1,2], Marangoni convection has been considered to be a fundamental research topic in fluid mechanics. An instructive review of contributions of early scientists to understand and study Marangoni convection can be found in [3]. Marangoni convection is widely considered to be more critical and important under microgravity conditions, where it can dominate heat and mass transfer processes due to the vanishing influence of buoyancy. Therefore, thermocapillary convection plays a fundamental role in material production processes in space [4]. Moreover, one can purposefully apply temperature gradients to move and eliminate bubbles or drops suspended in liquid materials [5,6], as well as in other applications like manufacturing of single-walled carbon nanotubes [7], monocrystal production, and investigating flame spread above liquid fuels [8], to mention only a few examples.

Different flow configurations are known in experimental studies of thermocapillary instabilities, which are due to externally imposed temperature gradients normal or parallel to the interface or the free surface of both simple and binary fluids [9,10]. An extensively used configuration to study thermocapillary flow under gravitational conditions is the surface-tension-driven convection around a gas bubble under a heated wall immersed in a liquid matrix subjected to an applied upward temperature gradient as shown in Fig. 1. In the 1960s and 1970s a couple of experimental and numerical studies dealing with this or similar flow configurations were conducted in order to understand the influence of thermocapillary convection on boiling heat transfer [11–15]. At relatively low-temperature gradients, a steady flow, characterized by an axisymmetric vortex, forms close to the air bubble interface and is followed by a secondary vortex and then further weak vortices below the bubble. The primary vortex was noticed to be smaller than the secondary one due to the coupling effect of both buoyancy and thermocapillary flow as observed in [16], for example.

Also, a similar experiment under reduced gravity in a sounding rocket flight was conducted in order to eliminate the gravitational influence on the surface-tension-driven flow [17]. Using thermochromic liquid crystal microspheres one observed the steady thermocapillary temperature and velocity field around the spherical bubble, which, due to the absence of gravity, did not show any secondary vortices. Analog experiments were carried out using shadowgraphy under variable gravitational conditions using parabolic flights [18]. They revealed periodic oscillatory thermocapillary flow behaviors at different gravity levels, where the frequency f of these oscillations was depending considerably on the gravity magnitude. On earth, for a 0.6 mPa s dynamic viscosity silicone oil as test liquid and a horizontal bubble diameter of about 8 mm, oscillatory movements of a frequency of 0.24 Hz were recorded visualized by generated interference fringes at vertical temperature gradients of more than 0.5 K/mm, [19]. These oscillations correspond to oscillatory instabilities

of density and thus temperature fields. With increasing temperature gradients of more than 1 K/mm (increasing Mg numbers), the oscillations were transmitted to a higher frequency mode of more than 0.6 Hz. Continuing this comprehensive experimental study, the effect of bubble sizes on the thermocapillary flow behavior was investigated [20]. Applying horizontal light sheet visualization, an annular ring, characterized by transient periodic deformations in the azimuthal direction, was noticed in the center of the secondary vortex below the bubble. The oscillations in the vertical direction were found to be weaker than the azimuthal ones. The authors pointed out that the Mg number, at which these oscillations changed from the periodic to a nonperiodic state, was different when varying the bubble aspect ratio r_B/z_B. Using the shadowgraph technique, one found three different periodic oscillation modes of the thermocapillary boundary contour around the injected air bubble [21]. This optical contour is a result of the refractive index variation of silicone oil with temperature and represents the boundary of the primary thermocapillary vortex. It was found that the critical Mg number $\mathrm{Mg_c}$, required to drive the flow into an oscillatory state, increases at higher bubble aspect ratios. In a similar experimental arrangement, transient temperature oscillations at a specific location near the injected air bubble were recorded [22]. The authors ascribed the reason of these oscillations to the subsequent reduction in the driving temperature gradient caused by the induced thermocapillary flow and the enhancement of the thermocapillary flow again through heat transfer by conduction leading to periodically oscillating flow. The oscillations changed from the periodic to a nonperiodic state by increasing the Mg number. In 2007, researchers observed the formation of small parasitic bubbles around the injected leading bubble at higher temperatures of the upper plate which disturbed the flow visualization and thus the temperature field evaluation using an interferometer [23]. According to the fact that the vaporization temperature of liquids increases with pressure, the authors suggested conducting future experiments at higher pressure conditions. This measure permits reaching higher temperatures and accordingly higher Mg numbers without disturbing evaporation effects at the interface.

As described above, previous studies focused on recording the critical values of the Mg number $\mathrm{Mg_c}$ where the oscillatory flow starts, at different bubble diameters for different fluids. However, no distinguished image of the nonperiodic oscillatory flow region at higher temperature gradients and aspect ratios has been provided yet, a regime that remained to be characterized in detail. Therefore, the intention of our study is to experimentally investigate the nonperiodic flow behavior beyond $\mathrm{Mg_{tran}}$ and to identify different modes the flow undergoes by increasing Mg until a developed turbulent surface-tension-driven convection arises. Generally, the flow phenomenon can be categorized into laminar, periodic oscillatory, and nonperiodic oscillatory flow, which we detected by the patterns of the tracer particle motion around the bubble using particle image velocimetry (PIV), the visualization of the transient behavior of the thermocapillary vortex boundary contour using the shadowgraph technique, and temperature fluctuation measurements at relevant flow field locations using a resistance temperature detector (RTD). These class B pt 100 temperature sensors provide a measuring tolerance of $\mathrm{R_0}$: $\pm\,0.12\,\%$ according to DIN EN 60751, where the temperature readings were recorded every 100 ms. Moreover, high-temperature gradient experiments were also pursued under excess pressures Δp using an appropriate pressure chamber. The implementation of the mentioned experiments under excess pressure conditions formed a methodology that permitted us to reach higher temperature gradients and thus Mg numbers.

II. DIMENSIONLESS NUMBERS AND CHARACTERISTIC PROPERTIES

The physical problem of the interaction between surface tension gradients and the induced thermocapillary velocity field can be distinguished by a force balance analysis at the interface between the liquid and gas in tangential and normal directions. The tangential force balance leads to the formulation of a characteristic velocity U. Neglecting the thermal diffusivity α and the dynamic viscosity η of the gas phase, $U = \frac{l}{\eta_l}\,|\partial\sigma/\partial T|\,|\partial T/\partial z|$ as a characteristic flow velocity has been used in our definition of the Mg number [19]; see below.

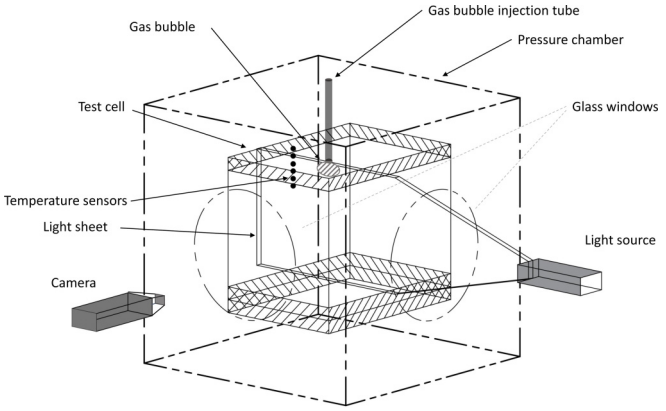

FIG. 2. Schematic of experimental setup with pressure chamber.

The flow can be characterised by the Mg number and the Prandtl number Pr, with $\mathrm{Pr} = \frac{\nu_l}{\alpha_l}$, where α_l, ν_l, and η_l denote the thermal diffusivity, kinematic viscosity, and dynamic viscosity of the liquid, respectively. The reference temperature for the temperature-dependent fluid properties was the one measured at an adequate reference point located near the bubble periphery ($r = 8.5$ mm, $z = 2.0$ mm). This is the position where we can approximately expect a mean stable reference temperature near the bubble vicinity, where our flow phenomenon takes place. A closer position of the reference temperature measurement to the bubble periphery could have influenced the heat transfer within the bubble vicinity taking into consideration a maximum horizontal radius of the injected air bubbles of 4.5 mm. The applied vertical temperature gradient $|\partial T/\partial z|$ is estimated through temperature sensors installed inside the test cell as shown in Sec. III. In the available literature, authors used the same criteria, which allows us to compare our data with findings of others. Eventually, Mg is defined in the following form: $\mathrm{Mg} = \frac{l^2}{\eta_l \alpha_l} |\partial\sigma/\partial T|\,|\partial T/\partial z|$. In our study, both the maximum horizontal bubble radius r_B and its vertical expansion z_B are used to define a characteristic length $l = (r_B z_B)^{\frac{1}{2}}$. For estimating Mg we used the measured undisturbed constant temperature gradient $|\partial T/\partial z|$ close to the heated wall. Thus, $\mathrm{Mg} = \frac{r_B z_B}{\eta_l \alpha_l} |\partial\sigma/\partial T|\,|\partial T/\partial z|$.

It should be noted that the bubble shape geometry is determined by its (air) volume and, due to buoyancy, is flattening in earthbound experiments when increasing its size. Therefore, under gravitational conditions no geometrical similarity is attainable when varying the bubble size.

III. EXPERIMENTAL SETUP AND METHODS

The heart of the experimental setup is the test cell shown in Fig. 2. It consists of a rectangular cavity of 50×80 mm^2 cross-sectional area and 15 mm height. Its top and bottom plates are made of 1.5-cm-thick copper plates with blackened surfaces, and its side walls are made of a single polycarbonate block, which allows one to carry out experiments at higher pressures and avoid any sealing problems caused by adhesives between the sidewalls. With the help of four corner screws, the upper and lower copper plates are tightly sealed to the glass walls by means of gaskets. The two plates are maintained at two different uniform temperatures T_w and T_c, respectively, to generate a vertical upward temperature gradient. The lower plate is cooled by means of a compact low-temperature thermostat using an ethanol-water mixture. The upper plate is heated using an electrical resistance heater. Six RTDs are inserted vertically at different distances from the upper plate close to the center to measure $|\partial T/\partial z|$ in the vicinity of the bubble. Regarding the applied temperature gradient in the z direction, we are fully aware of the fact that this value is modulated at the interface due to the different curvatures of the applied bubbles and the different flow states as well. The question of the instant temperature distribution on the surface is extremely difficult

to answer experimentally and could be a goal of numerical simulations which are not existing yet. For injecting an air bubble, a 1 mm diameter through hole is situated in the middle of the upper copper plate connected to a flexible plastic hose. The top plate contains two different through tubes for pressure equalization. As already mentioned we reached higher temperature gradients and thus Mg numbers without formation of disturbing liquid vapor bubbles by processing the experiments inside a pressure chamber as suggested in Fig. 2. It is in brief a cubical cell of internal side length 37 cm with four mountable steel lids. The upper boundaries and sidewalls consist of different sealed connection parts to access the utilities for heating and cooling the horizontal test cell plates, air valve control, pressurized air supply, bubble injection, and temperature and pressure measurements. The pressure chamber consists of two glass windows of optical quality for light accessibility of both the laser beam and the camera.

Conceptually, the experiments were simple. However, the preparation and execution of each experimental run proved to be relatively intricate. To carry out the trials the test cell was filled with the transparent low-viscosity silicone oil ($\nu = 0.65 \times 10^{-6}$ m^2/s at $T = 25\,^{\circ}$C, Pr $= 7.16$) as test liquid. Data for the values of ρ_l, α_l, ν_l, η_l, and σ were provided by Wacker Silicones. This test liquid was chosen for reaching high Mg values. Then, in the case of higher Mg numbers, the pressure chamber was pressurized to increase its pressure by Δp. After that, the temperature of the upper plate was increased until reaching T_w. When reaching a stable steady temperature gradient within the test liquid, the bubble was injected with an approximate air volume, and then, through analysis of the bubble images, its aspect ratio measured during each different experiment. The aspect ratio r_B/z_B measurement uncertainty was of the order of $\pm 2\%$. Two different optical techniques were used to give both qualitative and quantitative measurements of the fluid flow behavior. The optical setup used for the shadowgraph visualization of the thermocapillary vortex boundary contour formed around the injected air bubble is similar to the one used in [24] to prove that heat plumes initiate turbulence within a thermal convection. Since shadowgraphy is based on the refractive index contrast, it does not show directly the motions of the fluid but only those of "thermal objects" like plumes or thermal vortices. Thus, a boundary contour shows up due to differences in the refractive indices between the area of the disturbed temperature gradient near the bubble periphery because of the induced thermocapillary convective flow and the area of undisturbed stable temperature gradients relatively far from the flow area. The method consists of a collimated uniform light beam traversing the test cell and the liquid. The refractively deflected light ray appears brighter than the dark undeflected one on the camera sensor with spatial resolution of 1 mm = 82.7 pixel. More details on the shadowgraph technique can be found, for example, in [25]. For applying the PIV technique, the liquid inside the test cell was seeded with tracer particles made of small hollow glass spheres of mean diameter d_p of approximately $10\,\mu$m and density ρ_p of 1.1 g/l. To estimate that the particles follow the main flow without excessive slip, the calculated particle settling velocity U_∞, given by $U_\infty = \frac{d_p^2(\rho_p - \rho_l)}{18\,\eta_l}$ assuming that the Stokes law of drag is applicable, was estimated. The valuations show that U_∞ is less than 10% of the expected flow velocities of 0.1 mm/s in the case of steady laminar thermocapillary convection and less than 1% of the expected flow velocities of 0.1 cm/s in the case of nonperiodic thermocapillary convection. Moreover, we conducted some preliminary experiments using different types of tracer particles and found that the finally selected particles ensured a sufficient density matching. During the experiments no conspicuous rising or sinking of the particles to the top or bottom of the test cell could be observed. The test liquid was illuminated using a vertical laser light sheet of 3 mm thickness originating from a low-power laser source of 300 mW passing through the midplane of the test cell where the bubble was injected from the upper copper plate. The illuminated light sheet was shifted slightly behind the bubble tip surface to avoid any disturbing light reflections at the lower periphery of the bubble. Tracer images were then recorded using a CCD camera that was positioned perpendicular to the plane of illumination as shown in Fig. 2. A long-distance microscope was attached to the camera to provide adequate magnification and image resolution (1 mm = 316 pixel) within the available long working distance. Then these images were evaluated using appropriate software to generate velocity

vector field images. This software divides each recorded image into small interrogation areas. After that, by cross-correlation between two corresponding interrogation areas in subsequent images, a correlation map of tracer particle displacements was generated to gain a velocity vector flow field image. In general, PIV measurements were performed at moderate temperature gradients (Mg numbers) where the refractive index change is low and has no effect on the velocity measurements. To study the transient behavior of the flow, successive recordings of the shadowgraph images, PIV, and temperature measurements started just 30 s after injection of the air bubble to avoid any mechanical instability effects of the injection during the measurements. The observation time during the shadowgraphy measurements was approximately 90 s for each single experiment and began when the mechanical disturbances from the bubble injection decayed. The oscillation frequency of the periodic modes remained steady within this time. In the case of nonperiodic oscillations, we could not observe any qualitative change. Therefore, we considered an observation time of 90 s as sufficient. In total, we conducted about 800 experiments through the variation of both bubble aspect ratio in a range of 1.2 to 2.4 and temperature gradients up to 6.5 K/mm, respectively, resulting in a wide range of Mg numbers between approximately 10 000 and 140 000. We applied excess pressures up to 1.5 bar allowing us to reach the desired temperature gradients suppressing disturbing liquid evaporation. Only the most trustable measurements were then considered. For example, any mechanical disturbance leading to undesired movements of the bubble was a reasonable cause to discard this measurement. It should also be noted that the temperature, velocity, and shadowgraph measurements were pursued during separate experiments but at the same corresponding boundary conditions.

IV. RESULTS AND DISCUSSION

To start, different laminar flow vortex patterns around the injected air bubble at various boundary conditions were observed, where stable axisymmetric vortices showed up at lower Mg numbers and then, when increasing Mg, developed to form corresponding small vortices underneath the primary vortex, which then tends to migrate closer to the bubble. At temperature gradients above approximately 1 K/mm and different bubble diameters an onset of periodic oscillations was observed through the shadowgraph images. The thermocapillary flow vortices seem to reduce the driving temperature gradient, and then heat by conduction enhances the thermocapillary flow again leading to flow oscillations. Figure 3 shows the transient positions of the thermocapillary vortex boundary contour around the bubble visualized by shadowgraphy; Δt denotes the duration of each sequence displayed. Also, the transient velocity vector images, shown in Fig. 4, resulting from recordings of tracer particles under the same conditions show that the movements of the primary vortex, which does not disintegrate but changes its size, initiate these oscillations of the thermocapillary boundary contour. These patterns are displayed to give an impression of the fundamental periodic oscillation flow velocity fields. It should be noted, that due to light reflections on the bubble surface, which were eliminated using an imaging postprocessing tool, velocity vectors on the bubble periphery could not be generated. That justifies the lack of velocity vectors on the white zone around the bubble. The patterns of this recirculation zone repeated themselves in a periodic manner. The frequency of the boundary contour oscillations through shadowgraph images concurred well with the frequency of the velocity vector field. An interesting control measurement showed that the transient values of both the vertical velocity component at point A, located beneath the injected bubble ($r = 1.6$ mm, $z = 4.25$ mm), and the temperature measurements at point B, located beneath the upper plate but farther away from the bubble ($r = 8.5$ mm, $z = 4.0$ mm), displayed the same approximate frequency of 0.8 Hz as shown in Fig. 5. The slight difference in the value of the frequency could be justified as both PIV frequency and temperature measurement frequency were generated from two separate experiments with equal boundary conditions as mentioned before. The temperature measurement uncertainty was $\pm$ 0.01 K, which is around 10% of the displayed temperature fluctuations. The built-in temperature sensors were positioned about 8.5 mm radially away from the center line to enable experiments with larger bubbles. However, the PIV camera provided a smaller field of view

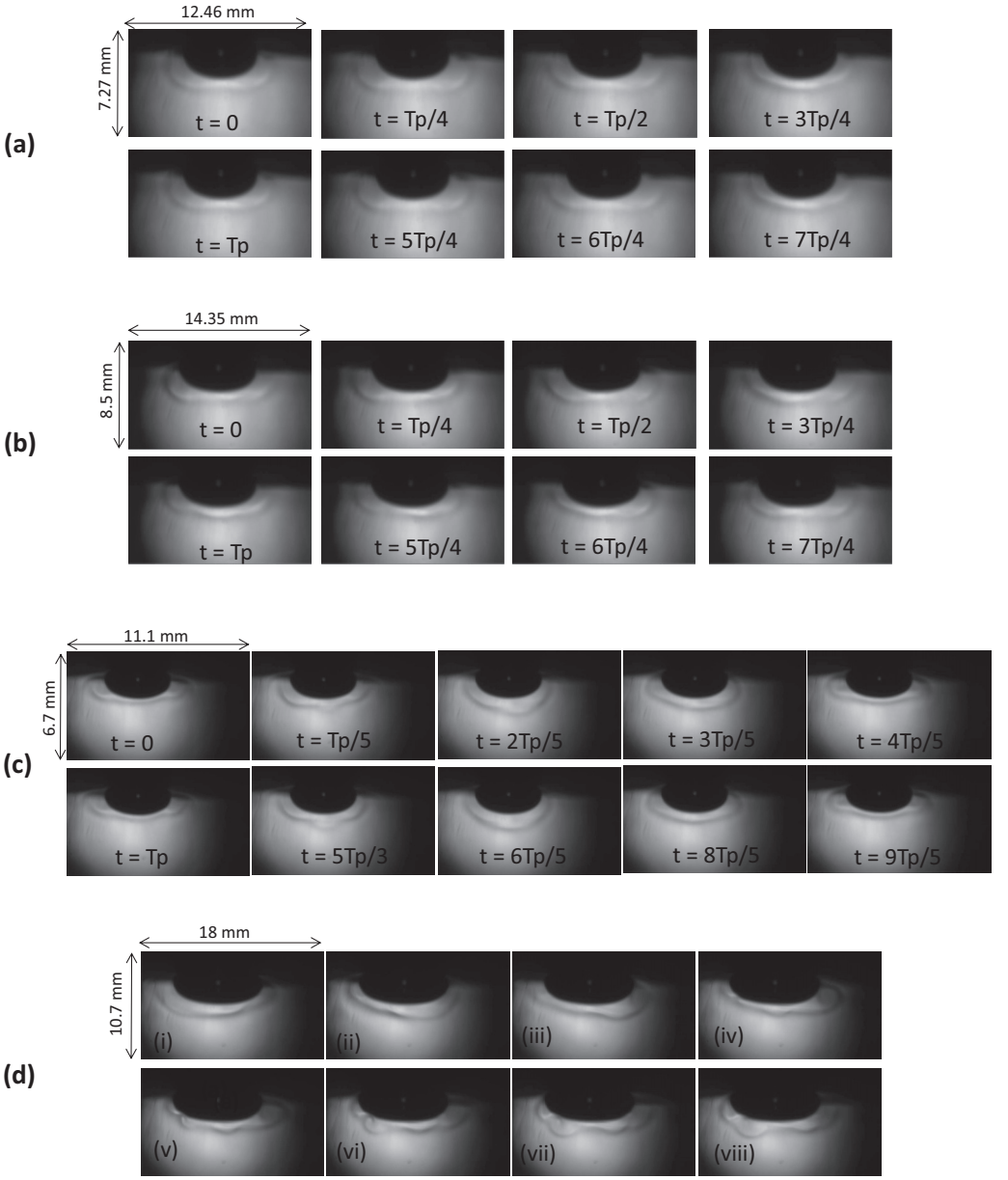

FIG. 3. Periodic modes below Mg_{tran} and transition to the first nonperiodic mode (phase A). (a) $r_B = 2.35\,\text{mm}$, $z_B = 2.2\,\text{mm}$, $|\partial T/\partial z| = 2$ K/mm, $\Delta p = 0\,\text{bar}$, Mg = 15 049, $f = 0.25$ Hz, and $\Delta t = 7$ s. (b) $r_B = 3$ mm, $z_B = 2.4\,\text{mm}$, $|\partial T/\partial z| = 1.6$ K/mm, $\Delta p = 0\,\text{bar}$, Mg = 16 330, $f = 0.28$ Hz, and $\Delta t = 6.25$ s. (c) $r_B = 3.2\,\text{mm}$, $z_B = 2.45\,\text{mm}$, $|\partial T/\partial z| = 2.33$ K/mm, $\Delta p = 0\,\text{bar}$, Mg = 26 800, $f = 0.8$ Hz, and $\Delta t = 2.25$ s. (d) $r_B = 4.44\,\text{mm}$, $z_B = 2.68\,\text{mm}$, $|\partial T/\partial z| = 2.33$ K/mm, $\Delta p = 0\,\text{bar}$, Mg = 40 700, and $\Delta t = 5$ s (phase A). Tp denotes the periodic time of oscillations.

of $5.6 \times 6.8\ \text{mm}^2$ beneath the upper plate for velocity measurements. That is why these velocity and temperature control measurements were conducted at different points. In the case of dominant periodic vertical oscillations, the flow field oscillations were homogeneous, such that both vertical velocity and temperature oscillations displayed the same frequency at different points beneath the

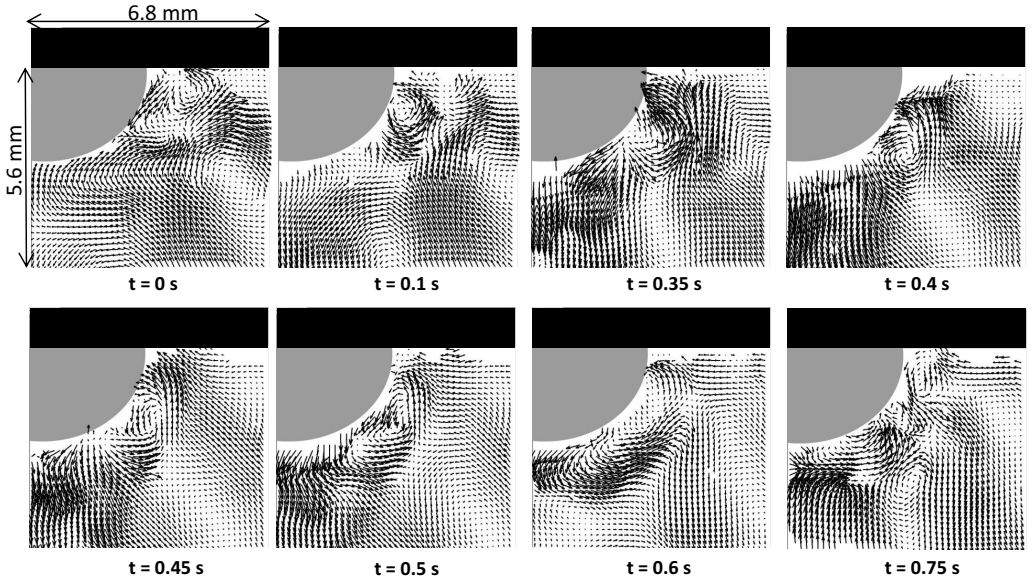

FIG. 4. PIV-measured velocity fields, $r_B = 3.2\,\text{mm}$, $z_B = 2.45\,\text{mm}$, $|\partial T/\partial z|$ =2.33 K/mm, $\Delta p = 0\,\text{bar}$, and Mg = 26 800.

bubble. The satisfying agreement between the integral results through shadowgraphy of Fig. 3(c) and quantitative results through velocity and temperature measurements displayed in Figs. 4 and 5 manifested the applicability of shadowgraphy to analyze the behavior of fluid flow and temperature fluctuations around the air bubble.

Different modes of boundary contour periodic oscillations were observed. Figures 3(a) and 3(b) show both periodic symmetric and asymmetric oscillations in the transverse direction, which were dominant compared to those in the vertical direction. At temperature gradients from 1 K/mm to 2 K/mm, these modes of horizontal periodic oscillations and frequencies between 0.2 and

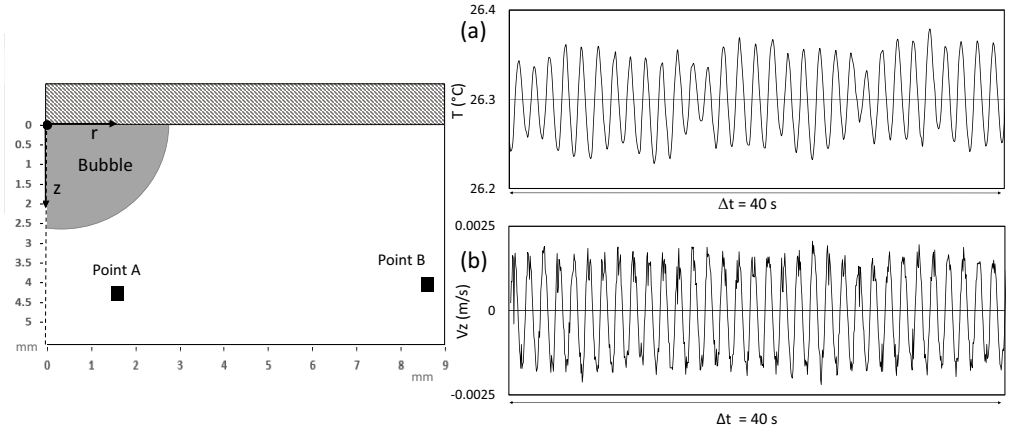

FIG. 5. (a) Typical temperature fluctuations at reference point B. (b) Typical vertical velocity fluctuations at reference point A ($r_B = 3.2\,\text{mm}$, $z_B = 2.45\,\text{mm}$, $|\partial T/\partial z| = 2.33$ K/mm, $\Delta p = 0\,\text{bar}$, Mg = 26 800, and $f \approx 0.8$ Hz).

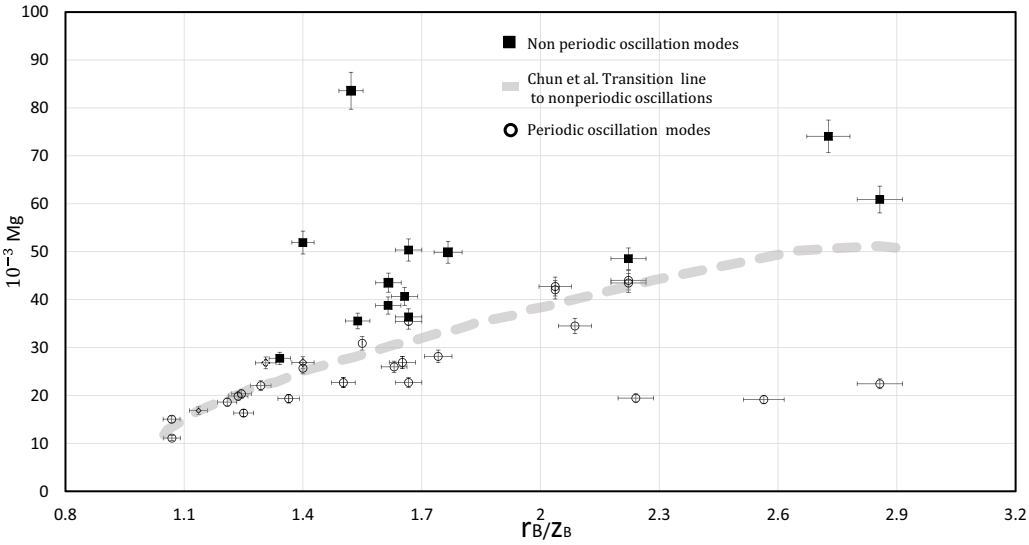

FIG. 6. Transition line of [20] and data of present study.

0.4 Hz were observed to be dominant. At a higher temperature gradient (Mg number) of about 2 K/mm, the vertical mode of periodic oscillations started to appear in the periodic oscillation region before reaching the transitional border to the nonperiodic oscillation domain. The frequencies of the vertical mode oscillations were found to be between 0.6 and 0.85 Hz being higher than the frequency of the horizontal oscillations. Moreover, these relatively higher frequency vertical periodic oscillations were dominant at temperature gradients above 2 K/mm regardless of the bubble sizes. Generally, our results within the periodic oscillation regime regarding the values of $\mathrm{Mg}_{\mathrm{tran}}$ for different bubble aspect ratios show satisfying agreement with previous results of [20] as shown in Fig. 6 and later. Each data point of Fig. 6 and following represents a mean result of five independent experiments on average with the same boundary conditions and a corresponding error bar. Figure 3(d) displays that at the same applied temperature gradient but at larger bubbles (higher Mg numbers), the behavior of the boundary contour oscillations changed to a nonperiodic mode (termed phase A) where some extra downward peak expansions are observed in the transverse direction. It was found that, at higher temperature gradients, these nonperiodic oscillations started to appear at smaller bubbles rather than at lower temperature gradients.

At about $\mathrm{Mg} > 65\,000$ and bubble aspect ratios between 1.0 and 2.0, the fluid flow velocities near the bubble periphery were measured. Due to relatively high velocities, higher frequency imaging with shorter capturing time was needed to adjust the PIV measurements. High-frequency imaging requires a more powerful light source particularly when using a long-distance microscope. However, in our experiments the maximum imaging frequency was about 50 Hz, where the tracer particles near the bubble interface displayed short lines instead of the default dot-shaped field. Therefore, the velocities near the bubble periphery were calculated manually with the same criteria of the displaced distance between two successive images. The corresponding velocity measurement uncertainty was $\pm 5\%$. The maximum fluid flow velocity magnitude $|U_{\mathrm{max}}|$ was detected near the bubble interface approximately 0.2 mm away from the bubble surface, where the fluid flow is initiated through the surface tension gradient. This confirms again that thermocapillarity is the principal driver of the flow and not buoyancy. Figure 7 shows the scaled thermocapillary flow driving velocity as a function of the bubble aspect ratio and the applied temperature gradient. Higher velocities were observed at larger bubbles at a given temperature gradient. The magnitude of the thermocapillary flow driving velocity determines the behavior of the thermocapillary flow field. First, the fluid particles on the bubble interface accelerate downwards because of the surface tension gradient. Then they decelerate

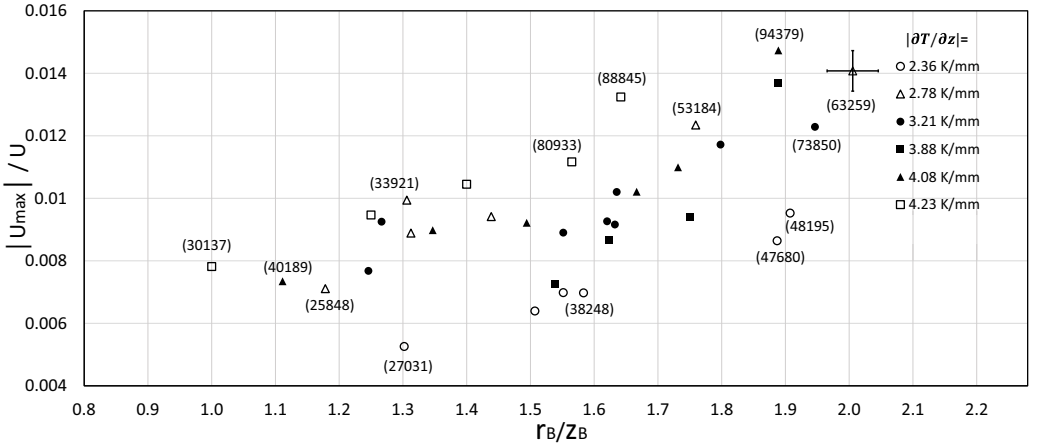

FIG. 7. Variation of the maximum flow velocity at the bubble surface with bubble shape at different temperature gradients. $|U|_{\max}$ is scaled with the characteristic flow velocity U. Parameters in brackets are Mg number values.

until they stop their motion at the pole of the bubble to reverse the movement upwards amplified by buoyancy. It was found that, at higher temperature gradients (higher Mg numbers), where the thermocapillary flow driving velocity is relatively high reaching a value of the order of 3 cm/s, the fluid particles on the bubble interface decelerate faster to enable reversing their movements at the end of the bubble interface. This sudden decrease in the velocities of the particles leads to flow instabilities and thus fast movements and interactions between flow vortices causing eventually a nonperiodic behavior of boundary contour oscillations as shown in Figs. 3(d) and 8, respectively.

At about Mg $>$ 80 000 the phase boundary between the bubble and the liquid became unstable due to vibrations of the bubble itself as its volume altered in a range of $\pm 5\%$.

The shadowgraph images of Fig. 8 illuminate the typical thermocapillary flow behavior we observed within the nonperiodic flow regime in some detail. Beyond the transitional Mg number, the thermocapillary flow undergoes different phases of nonperiodicity till reaching a highly developed turbulent state. Figure 8(a) shows a typical nonperiodic flow behavior at a Mg number just above $\mathrm{Mg}_{\mathrm{tran}}$, termed phase A, somewhat similar to the periodic oscillatory state in the vertical direction [shown before in Fig. 3(a)] except that the interactions between the boundary contour itself and the bubble interface formed a central peak at the boundary contour. When further increasing the Mg number, the fluid flow around the air bubble, termed phase B, displays a sudden side deformation leading to several simultaneous central peaks as shown in Fig. 8(b). These central peaks are modified and accompanied by fast successive transversely generated side pulses at a further increase of the Mg number as shown in Fig. 8(c), where both waves at the left and the right side are displayed. We termed this phase of nonperiodic oscillations phase C. Eventually, the fluid flow around the bubble undergoes phase D, which is characterized by a combination between fast side pulses in the horizontal direction and strong central peaks in the vertical direction. This phase of a developed turbulent thermocapillary flow is due to the formation of interacting oscillating vortices in both vertical and horizontal planes and is shown in Fig. 8(d). The black structures, displayed on the left in Figs. 8(a), 8(c), and 8(d), correspond to the installed temperature sensors and do not present any thermocapillary flow structure.

In summary, both periodic and nonperiodic modes of oscillations (shown in Fig. 8) were categorized by analyzing the generated image sequences of the shadowgraph measurements around the gas bubble. The analysis and classification are based on how continuous the thermal contour was, and therefore, the number of central peaks (N) were compared. Also, a criterion was how fast these central peaks propagate circumferentially. All the periodic oscillation modes were categorized

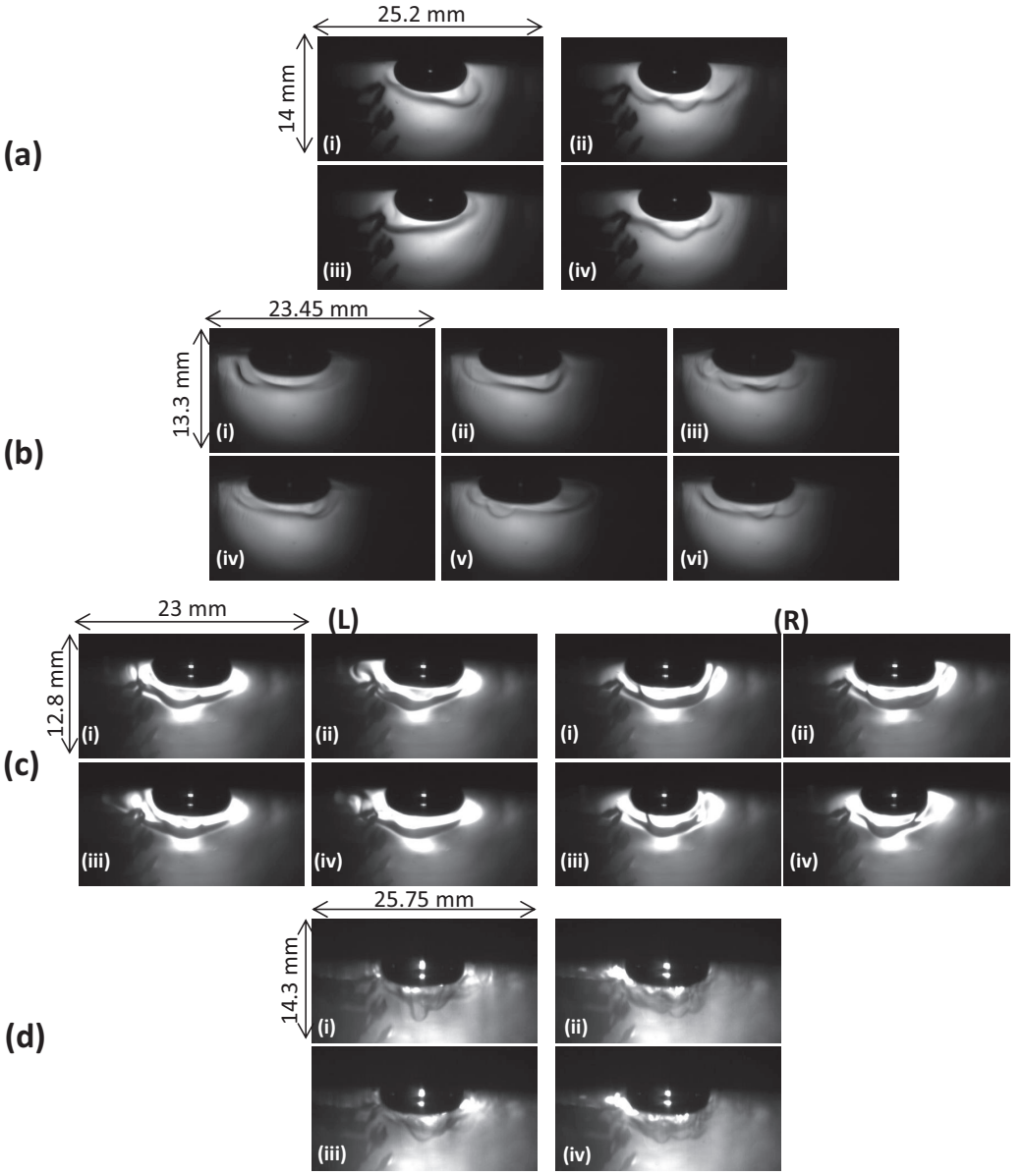

FIG. 8. Shadowgraph images of different modes of nonperiodic oscillations, (a) $r_B = 3.5\,\text{mm}$, $z_B = 2.5\,\text{mm}$, $|\partial T/\partial z| = 2.33\,\text{K/mm}$, $\Delta p = 0\,\text{bar}$, $\text{Mg} = 30\,100$, and $\Delta t = 2.5\,\text{s}$. (b) $r_B = 3.76\,\text{mm}$, $z_B = 2.53\,\text{mm}$, $|\partial T/\partial z| = 2.65\ \text{K/mm}$, $\Delta p = 0\,\text{bar}$, $\text{Mg} = 36\,385$, and $\Delta t = 2.5\ \text{s}$. (c) $r_B = 3.84\,\text{mm}$, $z_B = 2.55\,\text{mm}$, $|\partial T/\partial z| = 4.27\,\text{K/mm}$, $\Delta p = 1.2\,\text{bar}$, and $\text{Mg} = 69\,500$ (L: left side oscillations, $\Delta t = 0.85\,\text{s}$; R: right side oscillations, $\Delta t = 0.85\,\text{s}$). (d) $r_B = 4.41\,\text{mm}$, $z_B = 2.68\,\text{mm}$, $|\partial T/\partial z| = 4.96\ \text{K/mm}$, $\Delta p = 1.2\,\text{bar}$, $\text{Mg} = 101\,600$, and $\Delta t = 0.5\,\text{s}$.

by a continuous state of the thermal contour, $N = 0$; however, they are distinguished through the frequency of the oscillations. Phase A is categorized by only one central peak, $N = 1$. Phase B is categorized by the formation of multiple central peaks within the same period length, $2 < N < 5$. Phase C and phase B exhibit the same behavior regarding the number of central peaks; however, phase C shows remarkably faster side oscillations of an approximate mean oscillating frequency

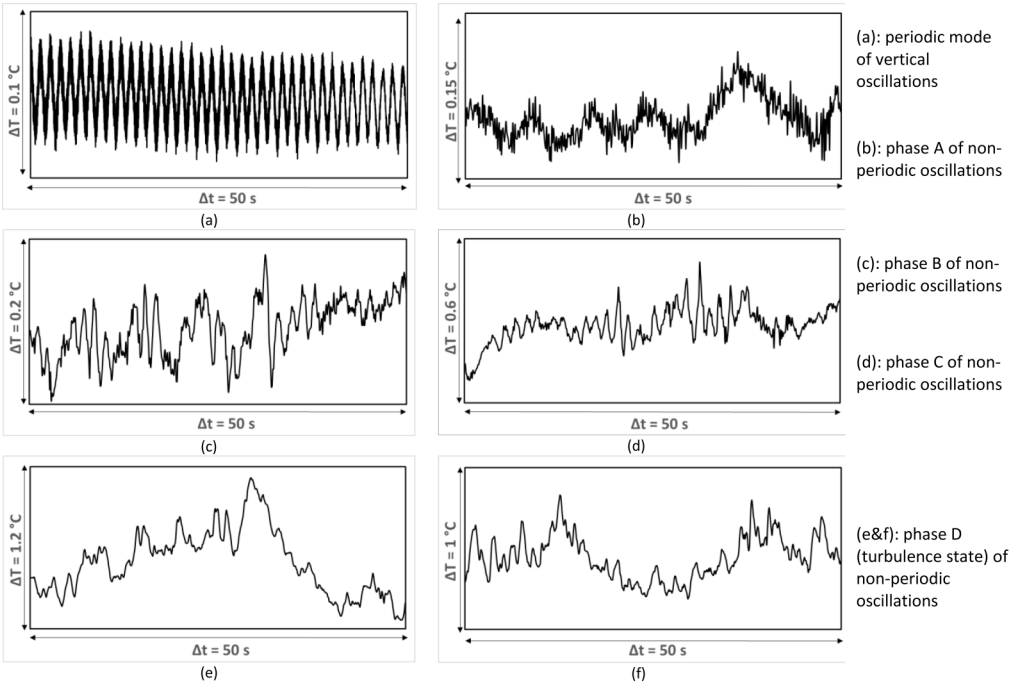

FIG. 9. Typical temperature fluctuation plots at the discrete point B for the different phases of the nonperiodic mode, $r_B = 4.5\,\text{mm}$, $z_B = 2.7\,\text{mm}$, (a) Mg = 35 450, $|\partial T/\partial z| = 1.96$ K/mm, $\Delta p = 0\,\text{bar}$, and $f = 0.67$ Hz. (b) Mg = 36 400, $|\partial T/\partial z| = 2.04$ K/mm, and $\Delta p = 0\,\text{bar}$. (c) Mg = 62 800, $|\partial T/\partial z| = 3.23$ K/mm, and $\Delta p = 1.5\,\text{bar}$. (d) Mg = 85 000, $|\partial T/\partial z| = 4.15$ K/mm, and $\Delta p = 1.5\,\text{bar}$. (e) Mg = 135 400, $|\partial T/\partial z| = 6.17$ K/mm, and $\Delta p = 1.5\,\text{bar}$. (f) Mg = 139 400, $|\partial T/\partial z| = 6.37$ K/mm, $\Delta p = 1.5\,\text{bar}$. Note different scalings of the temperature axis.

of up to 2 Hz. Phase D is considered as a more developed multicentral peak phase, where $N \geqslant 6$. Moreover, its side oscillations showed higher local frequencies.

Figure 9 shows comparable temperature plots of different flow modes when increasing Mg. The plot of Fig. 9(a) reveals a pure periodic fluid flow behavior within the periodic regime. After that, the nonperiodicity starts to appear at slightly higher Mg. Further increase in the Mg number increases the span of temperature variations ΔT as well as the disorder of temperature fluctuations.

In addition to that, using statistical methods, the data of the temperature fluctuation plots were analyzed to provide a more quantitative characterization of the disorder of the identified convective flow modes. The temperature field around the air bubble is affected by the thermocapillary fluid flow and thus the flow velocities and their fluctuations. Hence, we quantify the intensity of the fluctuations of the flow modes using the quantity T (fluid temperature). The mean temperature value $\overline{T}$ is defined by

$$\overline{T} = \frac{1}{n}\sum_{i=1}^{n} T_i.$$

With

$$T_i' = T_i - \overline{T}$$

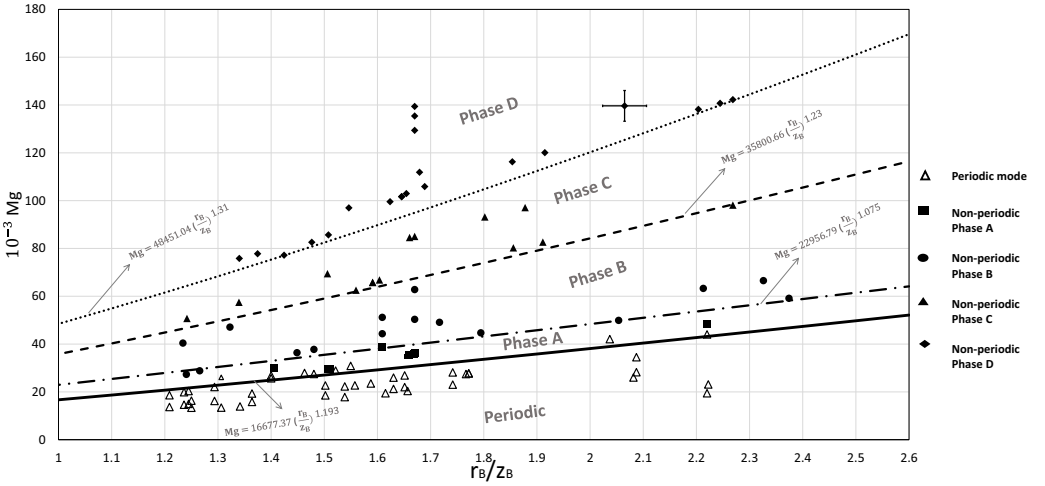

FIG. 10. Mg, (r_B/z_B) map: summary of measurements and classification of flow modes.

and

$$T'_{rms} = \sqrt{\frac{1}{n}\sum_{i=1}^{n}(T'_i)^2},$$

the turbulence intensity I (magnitude of turbulence) is defined as

$$I = \frac{T'_{rms}}{\overline{T}} \times 100\%,$$

where $\overline{T}$ denotes the average value of n discrete temperature measurements (T_i), T'_i the discrete temperature fluctuations, and T'_{rms} the root-mean-square value of temperature fluctuations.

The temperature oscillations [Fig. 9(a)] show a maximum value $T'_{\max}$ of about 0.04 K. That reveals a periodic thermocapillary flow behavior, which is noticeable in the corresponding temperature fluctuation plot. Figure 9(b) shows the start of the flows nonperiodicity, where the value of $T'_{\max}$ increases to 0.063 K leading to a turbulence intensity I of 0.084%. Further increasing the Mg numbers leads to upgrading the nonperiodic phase of fluctuations to higher modes. The temperature fluctuations of phase B [Fig. 9(c)] show a maximum value $T'_{\max}$ of about 0.09 K and a I of 0.09%. Furthermore, the temperature fluctuations of Fig. 9(d), which corresponds to phase C of nonperiodic oscillations, show higher values of $T'_{\max}$ and I of 0.18 K and 0.19%, respectively. Henceforth, the values of $T'_{\max}$ and I increase till reaching about 0.22 K and 0.32%, respectively; see temperature fluctuation plots of Figs. 9(e) and 9(f), which reveal a noticeable turbulence intensity of a developed turbulent thermocapillary flow.

The critical values of Mg numbers, needed to upgrade a nonperiodic phase of oscillation to the next higher one, depend on the temperature gradient and the bubble aspect ratio, which determines the shape (curvature) of the phase boundary (interface) between the two different phases (liquid and gas).

Figure 10 displays a summary of our experimental results in form of a Mg, (r_B/z_B) map. All experiments are comparable regarding the matrix liquid (silicone oil), dimension of the test cell, and boundary conditions. We varied only temperature gradients and bubble sizes. Figure 10 also indicates the boundary between periodic flow conditions and the nonperiodic ones. Moreover, it provides guideline borders between the periodic and the nonperiodic flow mode regimes (phases A–D). The measuring points were generated under variation of the bubble aspect ratio in a range

TABLE I. Values of power-law constants of the phase-transient border lines.

$i \rightarrow j$	A	n	Symbol
Periodic → Phase A	16 677.37	1.193	
Phase A → Phase B	22 956.79	1.075	
Phase B → Phase C	35 800.66	1.23	
Phase C → Phase D	48 451.04	1.31	

of 1.2 to 2.4 and the temperature gradient $|\partial T/\partial z|$ up to 6.5 K/mm (Mg between approximately 10 000 and 140 000).

As the measurement data of Fig. 10 suggest, a simple power law of the form $\mathrm{Mg}_{i\rightarrow j} = A\,(r_B/z_B)^n$ can be derived within the range of the measurement data in order to express the phase transient border lines in the form of empirical equations. Although the border lines of Fig. 10 look fairly linear, there is a tendency that the linearity diminishes with increasing Mg levels. The values of the corresponding constants A and n are given in Table I.

The trends of the power-law functions show that the first nonperiodic mode (phase A) takes place in a relatively narrow band of Mg versus r_B/z_B. The sectors of phases B, C, and D are rather wide, and their corresponding boundaries increase with increasing the exponent n, the value of which is given in Table I. It should also be noted, that for physical reasons, these transient border lines have to go through the origin of the plot Mg versus r_B/z_B (Fig. 10).

It is worth mentioning regarding the application of the presented power laws that if we used different fluid systems, we might find different wetting characteristics of this gas/liquid/solid system which would change the contact angle and with that the bubble shape and thus its aspect ratio. This could of course lead to errors when applying our power-law constants to other liquid-gas fluid systems. Another parameter influencing the bubble aspect ratio is the wetting characteristic of the solid wall. However, these issues were not within the scope of our study and have to await future investigations. Nevertheless, the trends we found in the thermocapillary flow behavior will qualitatively apply also for other fluid systems and wetting characteristics of the solid surface.

V. SUMMARY AND CONCLUSIONS

We experimentally studied both the periodic and nonperiodic oscillatory flow of the thermocapillary liquid convection around an air bubble under a heated wall under gravitational conditions, using a low viscosity liquid as working fluid. Shadowgraph and PIV techniques were applied to visualize the movement of the thermocapillary vortex boundary contour and characterize the flow behavior, respectively. Moreover, local temperature measurements delivered typical temperature fluctuation plots of the identified flow modes. We have been able to reach high Mg numbers by conducting the experiments under excess pressure conditions. The study reveals the origin of the boundary contour turbulent oscillations at high Mg numbers and shows how the fluid motion develops from a periodic oscillatory state to a nonperiodic state depending on the Mg number and the bubble aspect ratio. The PIV velocity vector field images show that the thermocapillary boundary contour oscillations are a result of the flow vortex movements and the variation of its size. We have observed three modes of periodic oscillations: (1) vertical oscillations, (2) transverse symmetric oscillations, and (3) transverse asymmetric oscillations and have shown the vertical periodic oscillatory state through both transient temperature and velocity measurements. Moreover, nonperiodic oscillations of the boundary contour were achieved at higher Mg numbers. The transitional temperature gradients, the $\mathrm{Mg}_{\mathrm{tran}}$ numbers, changed with the bubble aspect ratio. Our experiments reveal that in a large range of bubble sizes, the nonperiodic oscillatory state of the fluid flow around the gas bubble undergoes four different modes (A–D) depending on Mg and (r_B/z_B). The last one (phase D) is a developed turbulent state starting at Mg numbers of 75 000 for the smallest bubble aspect ratio

of $r_B/z_B = 1.2$ up to the maximum measured Mg number = 140 000 for a bubble aspect ratio of $r_B/z_B = 2.3$. These different phases were distinguished through various modes of the boundary contour fluctuations. In addition, thermocapillary flow driving velocities were measured at different boundary conditions (bubble sizes) close to the bubble surface. The data clearly reveal that it is the high magnitude of the interfacial velocity that initiates the interactions between thermocapillary flow vortices leading finally to the nonperiodic boundary contour oscillations, and hence buoyancy plays a secondary role in the described flow configuration. Eventually we could satisfactorily prove turbulent thermocapillary flow.

Many questions remain. It would be interesting to look at smaller bubbles of aspect ratios between 1 and 1.2, which become more spherical with decreasing size. This change of surface curvature would markedly influence the flow and temperature field. However, corresponding experiments within this aspect ratio range necessitate a completely newly reviewed measurement technique for the need of far higher image resolutions. Also, continuing experiments under low-gravity conditions would allow us to decouple buoyant convection from the surface-tension-driven one. We expect a far wider flow field due to thermocapillary convection under weightless conditions, as already shown for laminar convection at very low Mg numbers in a sounding rocket experiment [17]. Another important question is how the instant surface temperature gradient at the bubble periphery develops when increasing Mg. Experimentally, this information is extremely difficult to catch. Here numerical simulations could give an answer. However, resolution of the remaining problems will have to await further studies on the experimental as well as on the theoretical/numerical side.

ACKNOWLEDGMENTS

We gratefully acknowledge the support of this work by Deutscher Akademischer Austausch Dienst (DAAD) and the Egyptian Government under grant GERLS 2016. We thank Dr. X. Yang and Dr. S. Heitkam at the Helmholtz Zentrum Dresden Rosenndorf (HZDR) for their support in using their long-distance microscope in our experiments.

[1] J. Thomson, On certain curious motions observable at the surface of wine and other alcoholic liquors, Philos. Mag **10**, 330 (1855).

[2] C. G. M. Marangoni, Ueber die Ausbreitung der Tropfen einer Flüssigkeit auf der Oberfläche einer anderen, Ann. Phys. Chem **219**, 337 (1871).

[3] A. A. Nepomnyashchy, P. Colinet, and M. Velarde, in *Interfacial Phenomena and Convection*, 1st ed. (Chapman and Hall/CRC, New York, 2001).

[4] J. Aleksic, J. A. Szymczyk, A. Leder, and T. A. Kowalewski, in *Proceedings of the Thermocapillary and Forced Convection in Czochralski Crystal Growth Configuration, CMEM 2001, 4–6 Juni 2001, Alicante, Spain*, Computational Methods and Experimental Measurements X (WIT Press, 2001), pp. 627–636.

[5] G. Amberg and J. Shiomi, Thermocapillary flow and phase change in some widespread materials processes, Fluid Dyn. Materials Proc. **1**, 81 (2005).

[6] R. S. Subramanaian, R. Balasubramaniam, and G. Wozniak, Fluid mechanics of bubbles and drops, in *Physics of Fluids in Microgravity*, 1st ed., edited by R. Monti (CRC Press, London, 2002), pp. 149–177.

[7] S. H. Jin, S. N. Dunham, J. Song, X. Xie, J.-H. Kim, C. Lu, A. Islam, F. Du, J. Kim, J. Felts *et al.*, Using nanoscale thermocapillary flows to create arrays of purely semiconducting single-walled carbon nanotubes, Nat. Nanotechnol. **8**, 347 (2013).

[8] J. Cai, F. Liu, and W. A. Sirignano, Three-dimensional flame propagation above liquid fuel pools, Combust. Sci. Technol. **174**, 5 (2002).

[9] Y. Li, Experimental studies of Marangoni convection with buoyancy in simple and binary fluids, Ph.D. thesis, Georgia Institute of Technology, 2015.

[10] M. F. Schatz and G. P. Neitzel, Experiments on thermocapillary instabilities, Annu. Rev. Fluid Mech **33**, 93 (2001).

[11] J. L. McGrew, F. L. Bamford, and T. R. Rehm, Marangoni flow: An additional mechanism in boiling heat transfer, Science **153**, 1106 (1966).
[12] E. S. Gaddis, The thermal equilibrium of a vapour bubble on a heated solid surface, Ph.D. thesis, Manchester University, United Kingdom, 1968.
[13] B. K. Larkin, Thermocapillary flow around a hemispherical bubble, AIChe J. **16**, 101 (1970).
[14] V. Huplik and G. D. Raithby, Surface-tension effects in boiling from a downward-facing surface, J. Heat Transfer **94**, 403 (1972).
[15] Y. S. Kao and D. B. R. Kenning, Thermocapillary flow near a hemispherical bubble on a heated wall, J. Fluid Mech. **53**, 715 (1972).
[16] G. Wozniak and K. Wozniak, Buoyancy and thermocapillary flow analysis by the combined use of liquid crystals and PIV, Exp. Fluids **17**, 141 (1994).
[17] G. Wozniak, K. Wozniak, and H. Bergelt, On the influence of buoyancy on the surface tension driven flow around a bubble on a heated wall, Exp. Fluids **21**, 181 (1996).
[18] C. Reynard, R. Santini, and L. Tadrist, Experimental study of the gravity influence on the periodic thermocapillary convection around a bubble, Exp. Fluids **31**, 440 (2001).
[19] D. Raake, J. Siekmann, and C.-H. Chun, Temperature and velocity fields due to surface tension driven flow, Exp. Fluids **7**, 164 (1989).
[20] C.-H. Chun, D. Raake, and G. Hansmann, Oscillating convection modes in the surroundings of an air bubble under a horizontal heated wall, Exp. Fluids **11**, 359 (1991).
[21] C. Reynard, R. Santini, L. Tadrist, and P. Arlabosse, The experimental study of the periodic instability of thermocapillary convection around an air bubble, in *Proceedings of the Space Technology and Applications International Forum*, edited by M. J. Bragg and M. S. El-Genk, AIP Conf. Proc. No. 504 (AIP, Melville, 2000), p. 878.
[22] J. Betz and J. Straub, Numerical and experimental study of the heat transfer and fluid flow by thermocapillary convection around gas bubbles, Heat Mass Transfer **37**, 215 (2001).
[23] K.-P. Schade, G. Wozniak, and C. Gessenhardt, Experimental investigation of thermocapillary flow at the phase boundary of a bubble in a liquid, in *Proceedings of the 6th International Conference on Multiphase Flow, ICMF 2007, Leipzig, Germany, July 9–13, 2007* (2007), p. 1.
[24] H.-D. Xi, S. Lam, and K.-Q. Xia, From laminar plumes to organized flows: The onset of large-scale circulation in turbulent thermal convection, J. Fluid Mech. **503**, 47 (2004).
[25] W. Merzkirch, Optical flow visualization, in *Flow Visualization*, 2nd ed. (Academic Press, Orlando, Florida, 1987), pp. 115–231.